ACS Photonics

Article

pubs.acs.org/journal/apchd5

MEMS Tunable Mid-Infrared Plasmonic Spectrometer

Thomas Stark,[†] Matthias Imboden,[‡,§] Sabri Kaya,[‡,∥] Alket Mertiri,[†,⊥] Jackson Chang,[‡] Shyamsunder Erramilli,[#,○] and David Bishop*[,†,‡,#]

[†]Division of Materials Science and Engineering, Boston University, Brookline, Massachusetts 02446, United States

Departments of [‡]Electrical and Computer Engineering, [#]Physics, and [○]Biomedical Engineering, Boston University, Boston, Massachusetts 02215, United States

[∥]Department of Electrical and Electronics Engineering, Erciyes University, Kayseri 38039, Turkey

Supporting Information

ABSTRACT: We present a microelectromechanical systems (MEMS) tunable metamaterial, Fabry-Pérot interferometer with a widely tunable mid-infrared response. An array of subwavelength holes in a gold film is suspended above a gold reflector, forming an interferometer cavity whose length can be modulated over a range of 1.7 to 21.67 μm using MEMS electrostatic actuation. Reflectance spectra exhibit the convolution of extraordinary optical transmission through the holes and Fabry-Pérot resonances with free spectral ranges from 2900 to 230.7 cm^{-1}. Measuring the free spectral range enables us to perform in situ interferometric calibration of the cavity length. We present a simple analytical model that describes the experimental and simulated results. This device shows promise as a surface-enhanced sensing substrate with a tunable spectral response.

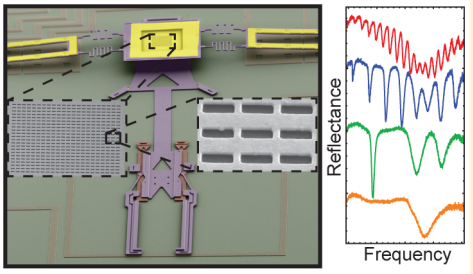

KEYWORDS: *metamaterials, plasmonics, extraordinary optical transmission, microelectromechanical systems, Fabry-Pérot*

Subwavelength holes in metal films have received considerable interest since Ebbesen et al. exhibited extraordinary optical transmission through an array of subwavelength cylindrical holes in a silver film.[1] Many experiments investigated the physical mechanism behind transmission, which is mediated by localized surface plasmons (LSPs) in the ridges of the holes and surface plasmon polaritons (SPPs) at the metal-dielectric interfaces.[1−6] The coupled SPPs and LSPs confine light to subwavelength dimensions, a phenomenon that has been exploited to enhance resolution of ultraviolet lithography in surface-plasmon-enhanced lithography.[7] The locally enhanced electric fields generated by subwavelength holes have been used to demonstrate a factor of 100 enhancement in infrared absorption of 1-dodecanethiolate[8] and a factor of 3.85 enhancement in Raman spectroscopy of rhodamine 6G.[9] In recent years, many technologies have been developed to tune the spacing between neigboring metamaterial elements, thereby tuning the electromagnetic coupling and spectral response.[10] For example, MEMS have been used to create tunable plasmonic metamaterials in the near-IR,[11] a tunable absorber in the infrared,[12,13] and tunable split ring resonators[14,15] and filters[16] in the THz regime. While subwavelength hole arrays have been used as sensing tools due to their electromagnetic field enhancement, tunable Fabry-Pérot interferometers have been used in sensing due to their narrow line widths and filtering capabilities, for example, to distinguish between the closely spaced spectral absorption features in alkane gases.[17,18] We present here a MEMS device that combines instruments of both types by integrating the electromagnetic response of a hole array with the tunability of a Fabry-Pérot interferometer. Because the mid-infrared properties can be modulated in a contollable manner, the device could be used in differential measurements and spectrometry applications.

The MEMS device presented here is fabricated using a hybrid approach that utilizes a commercial MEMS foundry[19,20] as well as postfoundry fabrication techniques. The MEMS device used in these experiments is shown in Figure 1a. A polysilicon frame supports a suspended gold film, in which an array of holes is fabricated using focused ion beam (FIB) milling,[21−27] as shown in Figure 1b. Two polysilicon and gold bimorphs, similar to those used to obtain large out-of-plane displacements in optical MEMS,[28] suspend the polysilicon frame 21.67 μm above the gold reflector. Here, we use two different rectangular hole geometries, the dimensions of which are defined in Figure 1c. Device 1 has design dimensions L = 1200 nm, W = 500 nm, P = 1600 nm, T_1 = 100 nm, and T_2 = 500 nm, while device 2 has design dimensions L = 1200 nm, W = 400 nm, P = 1600 nm, and $T_1 = T_2$ = 500 nm. While only two hole geometries are used here, the effect of hole geometry on the electromagnetic properties has been studied extensively by Ebbesen et al.[1] and García-Vidal et al.[5,29] Segmented electrostatic pull-down electrodes beneath the bimorphs in Figure 1a are used to deflect the bimorphs and change the cavity length d.

Received: May 28, 2015
Published: December 15, 2015

DOI: 10.1021/acsphotonics.5b00290
ACS Photonics 2016, 3, 14−19

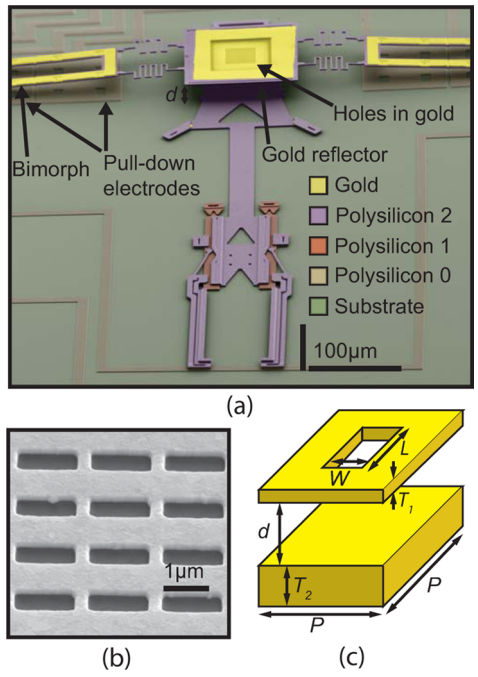

Figure 1. (a) False color SEM image of the MEMS and metamaterial–interferometer system. The foundry process consists of three polysilicon layers (polysilicon 0, polysilicon 1, and polysilicon 2) and one gold layer. (b) SEM image of the hole array in the suspended gold layer. (c) Schematic view of a unit cell of the array.

With the gold freely suspended by the polysilicon frame, this design has several advantages over suspended and on-substrate gold films used in previous works.[1,12,13,30] Hole arrays in suspended films are surrounded by a medium with a homogeneous dielectric background. It has been shown that plasmonic particles surrounded by a homogeneous dielectric background exhibit higher quality resonances than those fabricated on substrates.[31] It has also been shown that on-substrate hole arrays exhibit multiple resonances associated with having a nonuniform dielectric background.[1] Furthermore, the use of the polysilicon frame prevents straining the suspended gold film during actuation of the MEMS device. Previous works use a suspended gold film that bends when the device undergoes electrostatic actuation.[12,13,30] Thus, states in-between the unactuated state and the state in which the metamaterial is snapped down onto the bottom reflector exhibit artifacts due to the bending of the metamaterial. This hybrid fabrication approach using a MEMS foundry and FIB leverages the scalability and repeatability of the foundry and the customizability of FIB fabrication, allowing for a tunable general-purpose platform. A more detailed discussion of the device fabrication, including fabrication error and parallelism between the gold layers, can be found in the Supporting Information.

Optical characterization of the system was performed using a Fourier transform infrared (FTIR) spectrometer (Bruker Vertex 70 V) with a KBr beamsplitter coupled to an infrared microscope (Bruker Hyperion 1000) with Cassegrain reflection optics (15×, numerical aperture: 0.4) and a liquid nitrogen-cooled mercury cadmium telluride detector. Light was linearly polarized, defined using a knife edge aperture, and incident from above on an approximately 35 μm × 35 μm array of rectangular holes in the suspended gold. Reflected infrared spectra were collected over the range of 1000−5000 cm^{-1}, with 2 cm^{-1} resolution and 300 scans coadded. We modulated the length d of the cavity from 21.67 to 1.7 μm using MEMS electrostatic actuation, the details of which are discussed in the Supporting Information. We purged the microscope and surrounding air with dry, CO_2-scrubbed air to mitigate absorption by CO_2 and water.

The polarization dependence of the reflectance spectra is consistent with previous studies of transmission of light through arrays of subwavelength holes in metal films.[1,3,4,29,32] Figure 2a shows reflection spectra of device 1 for the maximum cavity length of 21.67 μm as the polarization direction is changed from the short axis to the long axis of the hole. When the polarization is along the short axis, the spectra show a broad dip in resonance, centered at 3820 cm^{-1} (red trace Figure 2a). Figure 2b shows that the reflectance minimum at 3820 cm^{-1} follows a $\sin^2(\theta)$ dependence on the polarization angle θ, evidence of the localized nature of the plasmon resonance.[4,32] The oscillations are the result of Fabry-Pérot resonances in the cavity between the hole array and the gold reflector.[33] The figure of merit typically used to describe a Fabry-Pérot interferometer is the finesse, defined as the ratio of the wavenumber spacing between the resonances (reflection minima in Figure 2a), or the free spectral range (FSR, ν_{FSR}), to the full width at half-maximum of the resonances.[34] It can be seen in Figure 2a that the Fabry-Pérot resonances near the plasmon resonance at 3820 cm^{-1} are of lower finesse than those further from it. Figure 4a shows that the reflectivity of the hole array is lowest at the 3820 cm^{-1} plasmon resonance and highest off-resonance. From Fabry-Pérot interferometer theory, it is

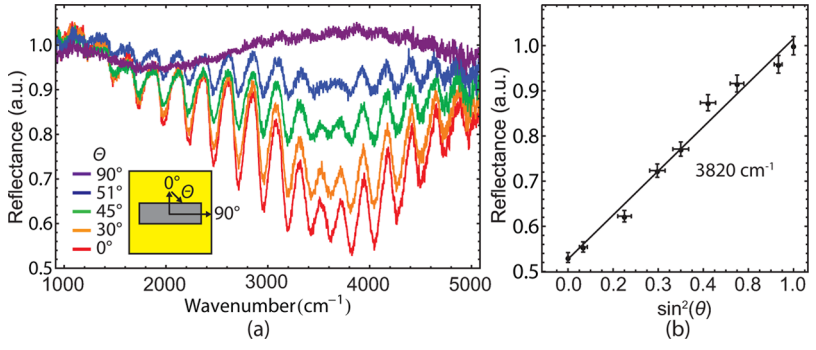

Figure 2. (a) Reflection spectra of device 1 for the maximum cavity length (21.67 ± 0.03 μm), as the polarization angle θ is changed from the short axis (θ = 0°) to the long axis (θ = 90°). (b) The reflectance at 3820 cm^{-1} as a function of $\sin^2(\theta)$. The linear fit has a coefficient of determination of R^2 = 0.98 and a slope of 0.49.

DOI: 10.1021/acsphotonics.5b00290
ACS Photonics 2016, 3, 14−19

expected that the high reflectivity (far from the plasmon resonance) corresponds to high finesse, while the low reflectivity (at the plasmon resonance) results in low finesse Fabry-Pérot resonances.[34] For polarization along the long axis of the hole, we expect a LSP resonance that is blueshifted from that for polarization along the short axis of the hole,[4,35] but it does not lie within the sensitivity range of the detector used in these experiments and hence is not detected.

The MEMS device enables us to change the cavity length, while the IR spectra enable us to perform in situ interferometric calibration of the cavity length. Figure 3a shows a series of

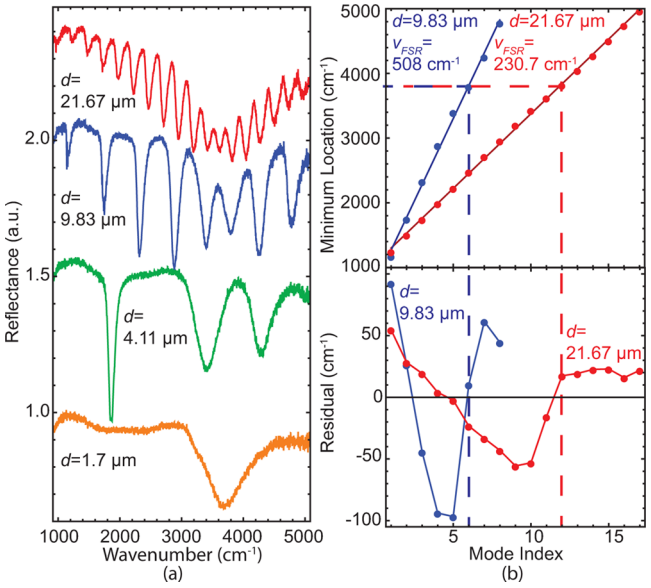

Figure 3. (a) FTIR spectra of device 1 for cavity lengths d of 1.7, 4.11, 9.83, and 21.67 μm. For clarity, the spectra are offset by −0.14, 0.40, 0.90, and 1.45 reflectance units, respectively. (b) Spectral reflectance minima locations as a function of mode index and the residuals from the linear fit.

FTIR spectra of device 1 as the cavity length is swept over the full available range. The polarization is fixed along the short axis of the hole. The relationship between the cavity length d and the FSR ν_{FSR} of a Fabry-Pérot interferometer surrounded by a medium of refractive index n is[34]

$$d = (2n\nu_{FSR})^{-1} \quad (1)$$

The FSR measured from the IR spectra in Figure 3a can be used to calibrate the cavity length by using eq 1. Figure 3b shows the Fabry-Pérot resonance minima as a function of mode index for the longest and second longest cavities shown in Figure 3a (top two spectra, red and blue traces, respectively). The slope of the best fit line in Figure 3b gives the FSR which, for the maximum cavity length, is 230.7 ± 0.3 cm^{-1}. Using this FSR and n = 1.00 for air[36] in eq 1, we obtain a cavity length d of 21.67 ± 0.03 μm. Similarly, for the second longest cavity, Figure 3b shows a FSR of 508 ± 1 cm^{-1}, which corresponds to a cavity length of 9.83 ± 0.02 μm and for the third longest cavity (third trace, green in Figure 3a, not included in Figure 3b) the FSR is 1215 ± 2 cm^{-1}, corresponding to a length d of 4.11 ± 0.01 μm. Independent measurements of the top three cavity lengths using a Zygo optical surface profilometer agree to within 4%. The cavity length of 1.7 ± 0.1 μm is measured with the optical surface profilometer; there is only one minimum in the frequency range shown, so the fitting method for interferometric height calibration used in Figure 3b can not be used.

The dashed lines in Figure 3b show that the zero crossing of the residuals approximately coincides with the spectral location and mode index of the reflectance minimum at 3820 cm^{-1}. Furthermore, the Fabry-Pérot resonance minima at lower frequencies than 3820 cm^{-1} are blue-shifted from the fit, while those at frequencies higher than 3820 cm^{-1} are red-shifted. This is the result of the convolution of Fabry-Pérot interferometer resonances with extraordinary optical transmission through the hole array, due to its plasmonic response.

We conducted finite difference time domain (FDTD) simulations for a hole array-interferometer system with the same design dimensions as device 1. Figure 4a shows FDTD-

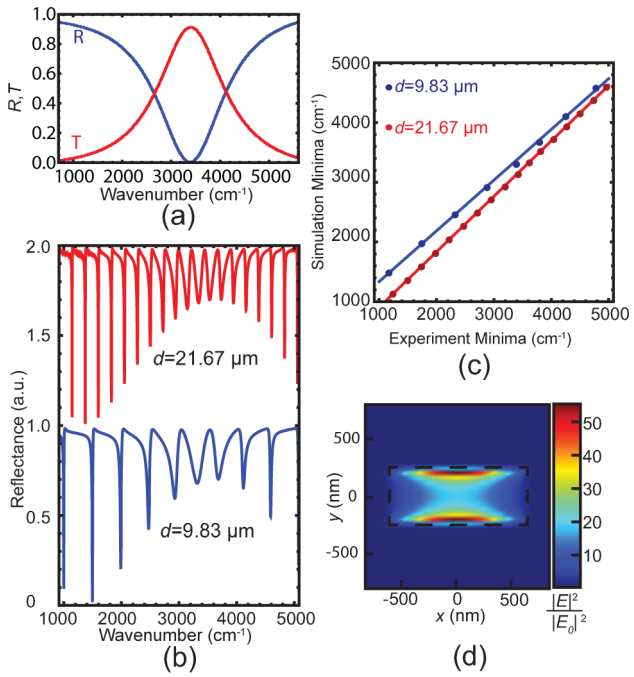

Figure 4. (a) FDTD simulations of reflectance from rectangular holes with the same design dimensions as device 1 (a) in a suspended, isolated (limit $d \rightarrow \infty$) gold film. (b) FDTD simulations of reflectance for cavity lengths d of 21.67 and 9.83 μm. For clarity, the d = 21.67 μm data has been shifted by 1.0 reflectance units. (c) Comparison of the simulated and experimental spectral minima locations for cavity lengths of 21.67 and 9.83 μm. (d) Simulated relative electric field intensity at 3377 cm^{-1} in a plane parallel to the hole at the hole center (limit $d \rightarrow \infty$). The dashed lines indicate the edge of the hole.

simulated reflectance and transmittance spectra for holes in an isolated (limit $d \rightarrow \infty$), suspended gold film, for radiation polarized along the short axis of the holes. The reflectance minimum occurs at 3377 cm^{-1}, which corresponds closely with the experimentally observed Fabry-Pérot resonance minimum at 3820 cm^{-1}. The simulations for d = 21.67 μm and d = 9.83 μm shown in Figure 4b recover the experimentally observed superposition of Fabry-Pérot interferometer resonances with extraordinary optical transmission through the holes. Figure 4c compares the spectral locations of the interferometer resonance minima for the experiment and simulation, for cavity lengths of 21.67 and 9.83 μm, and displays linear fits to these data. For a cavity length of 21.67 μm, the slope of the fit is 0.928, indicating good agreement between the free spectral range of

DOI: 10.1021/acsphotonics.5b00290
ACS Photonics 2016, 3, 14−19

the experimental and simulation data. Similarly, for a cavity length of 9.83 μm, the slope is 0.861. Figure 4d illustrates the simulated electric field intensity inside the hole in a plane parallel to the gold film at 3377 cm^{-1}. According to Figure 4d, the electric field intensity is enhanced by a factor of 55 in a plane through the hole center. It is the electric field enhancement of plasmonic structures that makes them valuable as surface-enhanced sensing substrates. For example, molecules adsorbed to the edge of the hole in Figure 4d would be perturbed by electric fields with intensities up to 55× that of the incident electric field.

A simple analytical model can be used to better understand the qualitative differences between the simulation and experiment. The analytical model considers a Fabry-Pérot interferometer,[34] in which the reflection coefficient of the gold reflector R_B is taken to be one and the reflection coefficient $\tilde{R}_H(\nu)$ and transmission coefficient $\tilde{T}_H(\nu)$ of the hole array are given by Lorentzian fits to the simulation data shown in Figure 4a:

$$|\tilde{T}_H(\nu)|^2 = \frac{|\tilde{E}_{T,H}|^2}{|\tilde{E}_0|^2} = \sqrt{\frac{c_T}{\pi}} \frac{\sqrt{\frac{\Gamma_T}{2}}}{(\nu - \nu_{0,T}) - i\frac{\Gamma_T}{2}} \times \text{c.c.} \quad (2)$$

$$= \frac{c_T}{\pi} \frac{\frac{\Gamma_T}{2}}{(\nu - \nu_{0,T})^2 + \left(\frac{\Gamma_T}{2}\right)^2} \quad (3)$$

and

$$|\tilde{R}_H(\nu)|^2 = \frac{|\tilde{E}_{R,H}|^2}{|\tilde{E}_0|^2} = \left(i - \sqrt{\frac{c_R}{\pi}} \frac{\sqrt{\frac{\Gamma_R}{2}}}{(\nu - \nu_{0,R}) - i\frac{\Gamma_R}{2}}\right) \times \text{c.c.} \quad (4)$$

$$= 1 - \frac{c_R}{\pi} \frac{\frac{\Gamma_R}{2}}{(\nu - \nu_{0,R})^2 + \left(\frac{\Gamma_R}{2}\right)^2} \quad (5)$$

Here, $\tilde{E}_{T,H}$ and $\tilde{E}_{R,H}$ are the complex electric field amplitudes transmitted through and reflected from the hole array and c.c. indicates the complex conjugate. The fit parameters are C_T = 2017 cm^{-1}, C_R = 2278 cm^{-1}, full widths at half-maximum Γ_T = 1359 cm^{-1}, Γ_R = 1450 cm^{-1}, and center frequencies $\nu_{0,T}$ = 3399 cm^{-1} and $\nu_{0,R}$ = 3377 cm^{-1}. The overall reflectance of the system is calculated by considering the electric field amplitudes reflected and transmitted at each interface and summing the geometric series of reflected amplitudes. The overall relative electric field amplitude $\tilde{E}(\nu)$ given by[34]

$$\tilde{E}(\nu) = G_R\tilde{R}_H + (G_T\tilde{T}_H)^2 R_B \exp(i\phi_B) \times \frac{\exp[i(4\pi nd\nu)]}{1 - G_R\tilde{R}_H R_B \exp(i\phi_B)\exp[i(4\pi nd\nu)]} \quad (6)$$

and the overall reflectance is

$$R(\nu) = \tilde{E}(\nu) \times \text{c.c.} \quad (7)$$

The parameters G_R and G_T represent the reflection and transmission losses, respectively, of the hole array and $\phi_B = \pi$ is a phase shift upon reflection from the gold reflector. The results based on this model are presented in Figure 5 and exhibit the convolution of Fabry-Pérot resonances with the inverted Lorentzian line shape of reflectance from the hole array. The

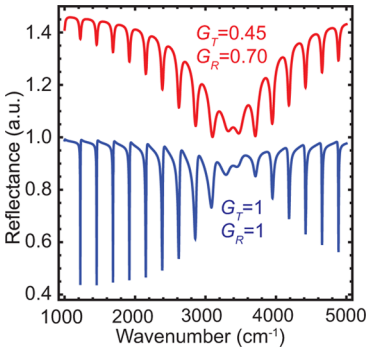

Figure 5. Reflection spectra obtained using the analytical model, for a cavity length d of 21.67 μm, and the reflectance and transmittance loss cofficients G_R and G_T shown. The G_T = 0.45, G_R = 0.70 plot is offset by 1.0 units for clarity.

spectrum without loss (G_T = 1, G_R = 1) in Figure 5 is more characteristic of the simulated spectrum in Figure 4b, exhibiting Fabry-Pérot resonance minima with a concave-down envelope. In the spectrum shown in Figure 5 that accounts for loss (G_T = 0.45, G_R = 0.70), G_T and G_R are manipulated to match the experimental spectra shown in Figure 2a and recover resonance minima that are contained by a concave-up envelope.

This analysis suggests that the simulation understates losses that occur in the experiment. The simulation considers an infinite array of holes, while the devices have 35 μm × 35 μm arrays of holes. Bravo-Abad et al. have shown that, for arrays with a small number of holes, the transmission per hole is far weaker for the holes near the edges of the array than those near the center while, for larger arrays, the transmission is stronger and more uniform across the array.[37] In addition, the simulations illuminate the array of holes with a perfect plane wave, whereas the experiment uses an objective with finite numerical aperture (NA = 0.4). Fabrication errors, such as the rounded corners and edge roughness visible in Figure 1b, would limit the experimental electric field intensity compared with the simulation. Furthermore, the thin film may have greater ohmic losses than the bulk, due to electron scattering at surfaces and grain boundaries.[38−40]

The locally enhanced electric fields in subwavelength metallic particles and holes have been used extensively in surface-enhanced sensing applications such as surface-enhanced Raman spectroscopy (SERS)[9] and surface-enhanced infrared absorption spectroscopy (SIERA).[8] Furthermore, it has been shown that arrays of plasmonic elements with uniform dielectric backgrounds, such as substrateless hole arrays[41,42] or particles embedded in a substrate,[31] exhibit higher quality resonances than those on substrates, making our device potentially valuable as a surface-enhanced sensing substrate. A typical surface-enhanced sensing substrate is fabricated to have a fixed geometry and static spectral response. By tuning the system geometry, the MEMS device presented here modulates the spectral response and shows potential for augmenting conventional surface-enhanced sensing techniques.

The integration of an interferometer with a metamaterial will enable this device to be used in a differential measurement mode, as shown in Figure 6a, for device 2. If, for example, a molecule with a vibrational band at 3650 cm^{-1} is adsorbed onto the suspended gold, the reflectance from the system can be varied between 0.82 and 0.35 with an estimated frequency of ~10 kHz[43] by tuning the cavity length. Combining this modulation with phase-sensitive detection methods will

DOI: 10.1021/acsphotonics.5b00290
ACS Photonics 2016, 3, 14−19

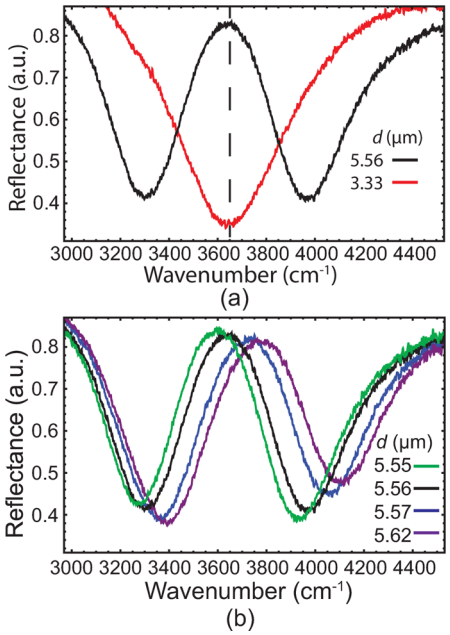

Figure 6. Reflection spectra for device 2 demonstrating how this device will be used in a differential measurement mode and (b) as a tunable plasmonic spectrometer.

considerably enhance signal-to-noise ratios. Additionally, this device could be used in a scanning mode by tuning the minimum or maximum across a frequency range of interest, as shown in Figure 6b. This would enhance the signal from one vibrational band, while suppressing that from others, thereby creating a tunable plasmonic spectrometer.

We have fabricated and characterized a MEMS tunable mid-infrared plasmonic spectrometer that combines the electromagnetic field enhancement and sensing capabilities of plasmonic structures with the tunability of a Fabry-Pérot interferometer. This technology promises to augment a class of plasmonic materials with fixed geometries that have already proven valuable as sensing substrates, as well as sensors based upon tunable Fabry-Pérot interferometers.[17,18] Used as a sensing substrate, the additional mechanical degree of freedom provided by the MEMS will enable dynamic tuning of the spectral response of the system, making this device a powerful tool for differential measurements and spectrometry.

■ ASSOCIATED CONTENT

Supporting Information

The Supporting Information is available free of charge on the ACS Publications website at DOI: 10.1021/acsphotonics.5b00290.

Additional figures and information on the MEMS fabrication process and MEMS mechanics (PDF).

■ AUTHOR INFORMATION

Corresponding Author

*Phone: +1 617 358-4080. Fax: +1 617 353-7337. E-mail: djb1@bu.edu.

Present Addresses

[§]Microsystems for Space Technologies Laboratory, École Polytechnique Fédéral de Lausanne, Neuchâtel, Neuchâtel 2002, Switzerland.

[⊥]Department of Biology, Boston University, Boston, Massachusetts 02215, United States.

Notes

The authors declare no competing financial interest.

■ ACKNOWLEDGMENTS

The authors gratefully acknowledge the support of the Defense Advanced Research Projects Agency Atoms to Product Program/Department of Defense/Air Force (FA8650-15-C-7545), Boston University, the National Institute of Health (NIH R21 EB013381-01), the National Science Foundation (NSF IIP-1068070 and NSF Grant No. 1361948), the Technological Research Council of Turkey (TUBITAK Project 115E209), and LGS Innovations. The authors thank Ronen Adato and Mi K. Hong for useful discussions.

■ REFERENCES

(1) Ebbesen, T. W.; Lezec, H. J.; Ghaemi, H. F.; Thio, T.; Wolff, P. A. Extraordinary optical transmission through sub-wavelength hole arrays. *Nature* **1998**, *391*, 667−669.

(2) Mary, A.; Rodrigo, S. G.; Martín-Moreno, L.; García-Vidal, F. J. Theory of light transmission through an array of rectangular holes. *Phys. Rev. B: Condens. Matter Mater. Phys.* **2007**, *76*, 195414.

(3) Ghaemi, H.; Thio, T.; Grupp, D.; Ebbesen, T. W.; Lezec, H. Surface plasmons enhance optical transmission through subwavelength holes. *Phys. Rev. B: Condens. Matter Mater. Phys.* **1998**, *58*, 6779−6782.

(4) Degiron, A.; Lezec, H.; Yamamoto, N.; Ebbesen, T. Optical transmission properties of a single subwavelength aperture in a real metal. *Opt. Commun.* **2004**, *239*, 61−66.

(5) García-Vidal, F.; Moreno, E.; Porto, J.; Martín-Moreno, L. Transmission of Light through a Single Rectangular Hole. *Phys. Rev. Lett.* **2005**, *95*, 103901.

(6) García-Vidal, F.; Martín-Moreno, L.; Moreno, E.; Kumar, L.; Gordon, R. Transmission of light through a single rectangular hole in a real metal. *Phys. Rev. B: Condens. Matter Mater. Phys.* **2006**, *74*, 153411.

(7) Pan, L.; Park, Y.; Xiong, Y.; Ulin-Avila, E.; Wang, Y.; Zeng, L.; Xiong, S.; Rho, J.; Sun, C.; Bogy, D. B.; Zhang, X. Maskless plasmonic lithography at 22 nm resolution. *Sci. Rep.* **2011**, *1*, 1−5.

(8) Williams, S. M.; Stafford, A. D.; Rodriguez, K. R.; Rogers, T. M.; Coe, J. V. Accessing Surface Plasmons with Ni Microarrays for Enhanced IR Absorption by Monolayers. *J. Phys. Chem. B* **2003**, *107*, 11871−11879.

(9) Xia, L.-P.; Yang, Z.; Yin, S.-Y.; Guo, W.-R.; Du, J.-L.; Du, C.-L. Hole arrayed metal-insulator-metal structure for surface enhanced Raman scattering by self-assembling polystyrene spheres. *Front. Phys.* **2014**, *9*, 64−68.

(10) Kanamori, Y.; Hokari, R.; Hane, K. MEMS for Plasmon Control of Optical Metamaterials. *IEEE J. Sel. Top. Quantum Electron.* **2015**, *21*, 1−10.

(11) Ou, J.-Y.; Plum, E.; Zhang, J.; Zheludev, N. I. An electromechanically reconfigurable plasmonic metamaterial operating in the near-infrared. *Nat. Nanotechnol.* **2013**, *8*, 252−255.

(12) Liu, X.; Padilla, W. J. Dynamic Manipulation of Infrared Radiation with MEMS Metamaterials. *Adv. Opt. Mater.* **2013**, *1*, 559−562.

(13) Pitchappa, P.; Ho, C. P.; Kropelnicki, P.; Singh, N.; Kwong, D.-L.; Lee, C. Micro-electro-mechanically switchable near infrared complementary metamaterial absorber. *Appl. Phys. Lett.* **2014**, *104*, 201114.

(14) Zhu, W. M.; Liu, A. Q.; Zhang, X. M.; Tsai, D. P.; Bourouina, T.; Teng, J. H.; Zhang, X. H.; Guo, H. C.; Tanoto, H.; Mei, T.; Lo, G. Q.; Kwong, D. L. Switchable magnetic metamaterials using micromachining processes. *Adv. Mater.* **2011**, *23*, 1792−1796.

(15) Zhang, W.; Liu, A. Q.; Zhu, W. M.; Li, E. P.; Tanoto, H.; Wu, Q. Y.; Teng, J. H.; Zhang, X. H.; Tsai, M. L. J.; Lo, G. Q.; Kwong, D. L. Micromachined switchable metamaterial with dual resonance. *Appl. Phys. Lett.* **2012**, *101*, 151902.

DOI: 10.1021/acsphotonics.5b00290
ACS Photonics 2016, 3, 14−19

(16) Han, Z.; Kohno, K.; Fujita, H.; Hirakawa, K.; Toshiyoshi, H. MEMS reconfigurable metamaterial for terahertz switchable filter and modulator. *Opt. Express* **2014**, *22*, 21326−21339.
(17) Mannila, R.; Tuohiniemi, M.; Antila, J. Hydrocarbon gas detection with microelectromechanical Fabry-Perot interferometer. *Proc. SPIE* **2013**, 1−9.
(18) Ebermann, M.; Neumann, N.; Hiller, K.; Seifert, M.; Meinig, M.; Kurth, S. Resolution and speed improvements of mid infrared Fabry-Perot microspectrometers for the analysis of hydrocarbon gases. *Proc. SPIE* **2014**, 1−9.
(19) Cowen, A.; Hardy, B.; Mahadevan, R.; Wilcenski, S. *PolyMUMPs Design Handbook*; MEMSCAP, 2011.
(20) PolyMUMPs by MEMSCAP, 2012; http://www.memscap.com/products/mumps/polymumps.
(21) Kim, S.; Latyshev, Y. I.; Yamashita, T. Submicron stacked-junction fabrication from Bi2Sr2CaCu2O8 + δ whiskers by focused-ion-beam etching. *Appl. Phys. Lett.* **1999**, *74*, 1156−1158.
(22) Enkrich, C.; Pérez-Willard, F.; Gerthsen, D.; Zhou, J.; Koschny, T.; Soukoulis, C. M.; Wegener, M.; Linden, S. Focused-Ion-Beam Nanofabrication of Near-Infrared Magnetic Metamaterials. *Adv. Mater.* **2005**, *17*, 2547−2549.
(23) Li, H.-W.; Kang, D.-J.; Blamire, M. G. Focused ion beam fabrication of silicon print masters. *Nanotechnology* **2003**, *14*, 220−223.
(24) Tseng, A. A.; Insua, I. A.; Park, J. S.; Li, B.; Vakanas, G. P. Milling of submicron channels on gold layer using double charged arsenic ion beam. *J. Vac. Sci. Technol., B: Microelectron. Process. Phenom.* **2004**, *22*, 82−89.
(25) Tseng, A. A. Recent Developments in Nanofabrication Using Focused Ion Beams. *Small* **2005**, *1*, 924−939.
(26) Huang, J.-S.; Callegari, V.; Geisler, P.; Brüning, C.; Kern, J.; Prangsma, J. C.; Wu, X.; Feichtner, T.; Ziegler, J.; Weinmann, P.; Kamp, M.; Forchel, A.; Biagioni, P.; Sennhauser, U.; Hecht, B. Atomically flat single-crystalline gold nanostructures for plasmonic nanocircuitry. *Nat. Commun.* **2010**, *1*, 150−158.
(27) Yao, N.; Epstein, A. K. Surface nanofabrication using focused ion beam. *Microscopy: Science, Technology, Applications and Education*; Formatex Research Center: Badajoz, Spain, 2010; Vol. *3*, pp 2190−2199.
(28) Wu, M. C. Micromachining for Optical and Optoelectronic Systems. *Proc. IEEE* **1997**, *85*, 1833−1856.
(29) Garcia-Vidal, F. J.; Martin-Moreno, L.; Ebbesen, T. W.; Kuipers, L. Light passing through subwavelength apertures. *Rev. Mod. Phys.* **2010**, *82*, 729−787.
(30) Noel, J.; Hijazi, Y.; Vlasov, Y. A. A switched high-Tc superconductor microstrip resonator using a MEM switch. *Supercond. Sci. Technol.* **2003**, *16*, 1438−1441.
(31) Adato, R.; Yanik, A. A.; Wu, C.-H.; Shvets, G.; Altug, H. Radiative engineering of plasmon lifetimes in embedded nanoantenna arrays. *Opt. Express* **2010**, *18*, 4526−4537.
(32) Gordon, R.; Brolo, A. G.; McKinnon, A.; Rajora, A.; Leathem, B.; Kavanagh, K. L. Strong polarization in the optical transmission through elliptical nanohole arrays. *Phys. Rev. Lett.* **2004**, *92*, 037401.
(33) Maier, S. A.; Friedman, M. D.; Barclay, P. E.; Painter, O. Experimental demonstration of fiber-accessible metal nanoparticle plasmon waveguides for planar energy guiding and sensing. *Appl. Phys. Lett.* **2005**, *86*, 071103.
(34) Saleh, B. E. A.; Teich, M. C. *Fundamentals of Photonics*; John Wiley & Sons, Inc.: Hoboken, NJ, 2007.
(35) Qiu, Y.; Zhan, L.; Xia, Y. Polarization-manipulated dual-band enhanced optical transmission through subwavelength rectangular hole array on metallic film. *IEEE J. Sel. Top. Quantum Electron.* **2013**, *19*, 4600106.
(36) Ciddor, P. E. Refractive index of air: new equations for the visible and near infrared. *Appl. Opt.* **1996**, *35*, 1566−1573.
(37) Bravo-Abad, J.; Degiron, A.; Przybilla, F.; Genet, C.; García-Vidal, F. J.; Martín-Moreno, L.; Ebbesen, T. W. How light emerges from an illuminated array of subwavelength holes. *Nat. Phys.* **2006**, *2*, 120−123.
(38) Mayadas, A. F.; Shatzkes, M. Electrical-Resistivity Model for Polycrystalline Films: the Case of Arbitrary Reflection at External Surfaces. *Phys. Rev. B* **1970**, *1*, 1382−1389.
(39) van Attekum, P.; Woerlee, P.; Verkade, G.; Hoeben, A. Influence of grain boundaries and surface Debye temperature on the electrical resistance of thin gold films. *Phys. Rev. B: Condens. Matter Mater. Phys.* **1984**, *29*, 645−650.
(40) Barmak, K.; Coffey, K. *Metallic Films for Electronic, Optical and Magnetic Applications: Structure, Processing, and Properties*; Woodhead Publishing, 2014; pp 440−453.
(41) Mattioli, F.; Ortolani, M.; Lupi, S.; Limaj, O.; Leoni, R. Substrateless micrometric metal mesh for mid-infrared plasmonic sensors. *Appl. Phys. A: Mater. Sci. Process.* **2011**, *103*, 627−630.
(42) Limaj, O.; Lupi, S.; Mattioli, F.; Leoni, R.; Ortolani, M. Midinfrared surface plasmon sensor based on a substrateless metal mesh. *Appl. Phys. Lett.* **2011**, *98*, 091902.
(43) Younis, M. I. *MEMS Linear and Nonlinear Statics and Dynamics*; Springer Science: New York, NY, 2011.

DOI: 10.1021/acsphotonics.5b00290
ACS Photonics 2016, 3, 14−19